Structural, optical and dielectric investigations of electrodeposited *p*-type Cu$_2$O

Mahdy M. Elmahdy[1,2] · **Abdelhamid El-Shaer**[3]

Abstract

Electrodeposition technique is employed to prepare cuprous oxide (Cu$_2$O) thin film on fluorine-doped tin oxide (FTO) conducting glass substrate through the reduction of copper lactate in alkaline solution at pH = 12.25. Structural, optical and dielectric properties of the prepared film is investigated by means of scanning electron microscopy (SEM), energy-dispersive X-ray spectroscopy (EDS), X-ray diffraction (XRD), UV–Visible absorbance, photoluminescence (PL) and broadband dielectric spectroscopy (BDS). The structural means (XRD, SEM and EDS) revealed the formation of self-assembled cubic microstructure of Cu$_2$O with average grain size of around 1.5 μm. The UV–Vis absorbance spectrum gives optical band gap of 2.05 eV. The PL spectrums confirmed the presence of defect centers ascribed to various forms of oxygen (V_O^{1+}, V_O^{2+}) and copper (V_{Cu}^{1+}) vacancies which are responsible for the conduction in the Cu$_2$O film. The conduction mechanism in the Cu$_2$O film is successfully described by the correlated barrier hopping (CBH) model in which bipolaron hopping become prominent. The density of defect states N, the effective barrier height W and the hopping distance R_ω are also calculated based on the CBH model. Two dielectric relaxation processes (β_1 and β_2) with Arrhenius temperature dependence and activation energies of 0.31 and 0.48 eV are observed. The fast β_2-relaxation process with activation energy of 0.48 eV is attributed to the Maxwell–Wagner-Sillars (MWS) polarization while the slow β_1-relaxation process with activation energy of 0.31 eV is due to the hopping of the oxygen and copper vacancies.

1 Introduction

Cuprous oxide (Cu$_2$O) is a *p*-type semiconductor with direct energy band gap of 2.2 eV at room temperature [1]. Its electrical conductivity owed to the presence of copper vacancies V_{Cu}^+. It has been the subject of numerous experimental and theoretical studies, but still its atomic and electronic structures continue to puzzle the researchers. It is nontoxic, low cost and has abundant source materials. Cu$_2$O has gained a renewed interest for several technological applications as chemical industry [2], biosensors [3] lithium ion batteries [4, 5] photo catalysis [6], photoluminescence [7], optoelectronic [8], gas sensors [9] and the fabrication of high efficiency solar cells [10–12].

Amongst a variety of synthesis methods available [13–24], none possesses the simplicity of Cu$_2$O electrodeposition which was first developed by Stareck [25]. This method is essentially a careful cathodic reduction of an alkaline solution of a cupric complex salt to form thin and uniform films of Cu$_2$O [26, 27]. It remains a more applicable procedure due to its simplicity, versatility, cost-effectiveness, controllability, direct control of film thickness and carried out at ambient pressures and temperatures.

Extensive theoretical and experimental studies of the optical properties and electronic structure of Cu$_2$O have been performed, including Auger electron spectroscopy [28], photoelectron spectroscopy (PES) [29, 30], optical adsorption and photoluminescence spectroscopy [31, 32], Infrared and Raman spectroscopy [33], neutron scattering [34, 35], local and semi-local functionals of density functional theory (DFT) based calculations, Hartree–Fock calculations and hybrid exchange formalism [36, 37].

The morphologies, shape of the crystals and crystal orientation of the Cu$_2$O can be controlled by adjusting the pH,

✉ Mahdy M. Elmahdy
  elmahdy@mans.edu.eg

1 Department of Physics, College of Science and Humanities in Al-Kharj, Prince Sattam Bin Abdulaziz University, Al-Kharj 11942, Saudi Arabia

2 Department of Physics, Faculty of Science, Mansoura University, 35516 Mansoura, Egypt

3 Department of Physics, Faculty of Science, Kafrelsheikh University, 33516 Kafrelsheikh, Egypt

amount of additives, temperature and type of substrates [38, 39]. Recent study by Das et al. [39] showed that the large grained Cu_2O thin film with reduced grain boundary cross-section leads to a significant enhancement in the photocurrent up to 30%. Large grained CdTe and perovskite based solar cells have also demonstrated high performance due to exhibiting excellent charge carrier mobility [40, 41].

The type of substrate can strongly influence the film structure, morphology and optical properties. It has shown that electrodeposited Cu_2O films on silicon, indium tin oxide (ITO), gold and FTO substrates demonstrate different structural, optical and growth dynamics [42, 43]. More recently, the impact of temperature, pH and deposition time on the structure of Cu_2O thin films has been reported [44] and found that the increase of pH leads to a change in the orientation of the (111) plane to (200) plane.

Investigating photoluminescence (PL) properties of semiconductors is of fundamental importance to understand relaxation processes of excited states out of equilibrium. The PL spectra of photo-excited Cu_2O at 3.05 eV have been recently reported [45] and found three features related to the blue, violet and yellow excitons.

Defects at the grain boundaries in addition to the interfacial effect have a significant influence on the electrical properties of thin film semiconductors. Dielectric relaxation spectroscopy is an extraordinary powerful tool for the investigation of the nature of defect centers by measuring the dielectric response over an extremely broad temperature (-160 to 250 °C) and frequency range (3μHz to 10 MHz) [46]. Few researchers have studied the dielectric properties of copper oxide, even though the AC-conduction mechanism is still lacking [47–51]. Sarker et al. have reported high dielectric permittivity in the lead-free polycrystalline CuO [48]. Moreover, Deepthi et al. [49] and Koshy et al. [47] have investigated the conduction mechanism of CuO nanostructure based on the CBH model. The conduction mechanism related to short and long range hopping of charge carriers was also reported for the electrodeposited Cu_2O/ZnO heterojunction on flexible ITO substrates [52].

In the present study, electrodeposition technique is employed to prepare thin film of Cu_2O deposited on FTO substrate at pH value of 12.25. The structural and optical investigations of the prepared film are conducted by X-ray diffraction (XRD), scanning electron microscopy (SEM), energy-dispersive X-ray spectroscopy (EDS) and photoluminescence (PL) while broadband dielectric spectroscopy (BDS) is used to explore the relaxation rates and conductivity in wide frequency (0.1 to 20 MHz) and temperature (153 to 393 K) ranges. The analysis of the dielectric spectra with the Havriliak–Negami (HN) model demonstrates two relaxation processes with Arrhenius temperature dependence and activation energies of 0.31 and 0.48 eV. The conductivity measurement reveals that the correlated barrier hopping (CBH) is the dominant conduction mechanism in the Cu_2O film. The PL spectrum confirms the presence of defect centers, which are responsible for the conduction in the Cu_2O film.

2 Experimental

2.1 Synthesis of Cu_2O thin film

Three-electrode setup was used for the electrodeposition of Cu_2O thin film. It consists of platinum wire as a counter electrode; Ag/AgCl as a reference electrode and fluorine doped tin oxide (FTO) coated glass substrate with size of 1×2 cm^2 as a working electrode. Cleaning of substrates was done by successive sonication for 10 min in isopropanol, acetone and then with deionized water. Finally, the cleaned substrates were dried in vacuum oven at 110 °C for about 30 min. The Cu_2O thin film was electrodeposited on FTO coated glass substrate using electrolyte solution consisting of 0.4 mol copper sulfate anhydrous ($CuSO_4$, 99.5%, BDH) and 3 mol lactic acid ($C_3H_6O_3$, 90%, AppliChem). The temperature of the electrolyte was fixed at 60 °C. The electrolyte solution was regulated at pH = 12.25 by adding 4 mol sodium hydroxide (NaOH, 99%, Oxford). Electrochemical deposition was carried out potentiostatically at applied voltage of -0.4 V between the working electrodes versus the Ag/AgCl reference electrode using the Bio-LogicSb-50 potentiostat. The deposition time was 30 min. As a final step, the deposited film was cleaned by deionized water and then dried with air flow.

The film thickness of the prepared film was determined by employing cross section observation by scanning electron microscopy (SEM). The side view of a cleaved Cu_2O film (Fig. 2b) show a film thickness of about 2.5 μm.

2.2 Characterization of Cu_2O thin film

Scanning electron microscope (SEM) (JEOL-6700F) at operating voltage of 5 kV was employed to investigate the surface morphology of the Cu_2O thin film. SEM-coupled energy-dispersive X-ray spectroscopy (EDS) technique for elemental analysis was performed at the same operating voltage. X-ray diffraction (XRD) analysis was measured using XRD-6000 Shimadzu diffractometer operating at 40 kV tube voltage and 30 mA current to generate Cu-K$_{\alpha 1}$ radiation with a wavelength of 1.54 Å. The measurements were recorded in the 2θ geometry between 10 to 60°. Absorption spectra in UV–Visible were recorded by a Jasco Co.V 630 double beam spectrophotometer at room temperature in a spectral range of 300 to 1100 nm. The photoluminescence (PL) spectra of the Cu_2O film were measured in the temperature range from 14 to 300 K using closed cycle Helium cryogenic. The film was excited by 325 nm

line of a He–Cd laser (Kimmon, IK5652R-G) resolved with a 320 mm monochromator (HORIBA, iHR320) and detected by a CCD (HORIBA, Symphony II) detector over a scanning range of 350 to 1000 nm.

2.3 Dielectric spectroscopy (DS)

Dielectric measurements were carried out using a Novocontrol BDS system composed of a broadband dielectric converter and a frequency response analyzer (Solartron Schlumberger FRA 1260). The measurements were performed in a frequency range of 1×10^{-1} to 2×10^{7} Hz and a temperatures range of 153 to 393 K. The sample temperatures were controlled in a nitrogen jet using a Quatro controller with stability better than 0.1 K.

A thin aluminum foil (thickness ~ 800 nm) with a diameter of 6 mm was used to form the top electrode for the Al/Cu$_2$O/FTO sandwich structure. The Cu$_2$O film thickness was ~ 2.5 μm. The complex dielectric permittivity ($\varepsilon^* = \varepsilon' - i\varepsilon''$, where ε' and ε'' are the dielectric constant and dielectric loss, respectively) is frequency ω and temperature T dependence. The Havriliak–Negami (HN) function including the conductivity term ($\sigma_0/i\varepsilon_0\omega$, σ_0 is the DC-conductivity and ε_0 is the permittivity of free space) (Eq. 1) was used to analyze the dielectric relaxation processes in wide frequency and temperature range [46].

$$\varepsilon^*(\omega) = \varepsilon_\infty + \sum_j \frac{\Delta\varepsilon_j}{\left[1 + \left(i\omega\tau_{jHN}\right)^{\alpha_j}\right]^{\gamma_j}} + \frac{\sigma_0}{i\varepsilon_0\omega} \tag{1}$$

where ε_∞ is the permittivity at high frequency, τ_{HN} is the HN relaxation time and $\Delta\varepsilon = \varepsilon_s - \varepsilon_\infty$ is the dielectric relaxation strength with $\varepsilon_s = \lim_{\omega\tau \ll 1} \varepsilon'(\omega)$ and $\varepsilon_\infty = \lim_{\omega\tau \gg 1} \varepsilon'(\omega)$. The shape parameters α and γ ($0 < \alpha, \alpha\gamma \leq 1$) in Eq. (1) describe the symmetrical and asymmetrical broadening of the complex dielectric function ε^*.

The fitting parameters (α, γ and τ_{HN}) obtained from Eq. (1) were used to calculate the relaxation time at maximum loss, τ_{max}, analytically as follows:

$$\tau_{max} = \tau_{HN} \left[\frac{\sin\left(\frac{\pi\alpha}{2+2\gamma}\right)}{\sin\left(\frac{\pi\alpha\gamma}{2+2\gamma}\right)} \right]^{-1/\alpha} \tag{2}$$

The values of τ_{max} follow the Arrhenius temperature dependence given in Eq. (3).

$$\tau_{max} = \tau_0 \exp\left(\frac{E}{k_B T}\right) \tag{3}$$

where τ_0 is the relaxation time at high temperature, E is the activation energy and k_B is the Boltzmann constant.

The complex functions of conductivity $\sigma^*(\omega)$ and electric modulus $M^*(\omega)$ are related to the complex dielectric function $\varepsilon^*(\omega)$ through the following relations [46].

$$\sigma^*(\omega) = \sigma' + i\sigma'' = i\omega\varepsilon_0\varepsilon^*(\omega) \tag{4}$$

$$M^*(\omega) = \frac{1}{\varepsilon^*(\omega)} = M' + iM'' = \frac{\varepsilon'}{\varepsilon'^2 + \varepsilon''^2} + i\frac{\varepsilon''}{\varepsilon'^2 + \varepsilon''^2} \tag{5}$$

where σ' and M' are the real parts of conductivity and electric modulus, respectively, while σ'' and M'' are the imaginary parts. The electric modulus was proposed as an analogy to the mechanical modulus in the viscoelastic relaxation of polymers [53]. Sometimes, the large values of the dielectric constant ε' and dielectric loss ε'' overwhelm the relaxation peaks which makes the deconvolution a very difficult task. This problem is completely eliminated in the electric modulus representation. The Havriliak–Negami (HN) function for the corresponding complex electric modulus is given by [46].

$$M^*_{HN}(\omega) = M_\infty + \frac{\Delta M}{\left[1 + \left(-i\left(\omega\tau_{HN-M}\right)^{-1}\right)^\alpha\right]^\gamma} \tag{6}$$

where $\Delta M = M_s - M_\infty$ is the electric modulus strength with $M_s = 1/\varepsilon_s$ and $M_\infty = 1/\varepsilon_\infty$.

Herein, the relaxation times and shape parameters are extracted from both ε^* and M^* representations.

3 Results and discussion

3.1 Structure and morphology

Crystal structure of the as-prepared Cu$_2$O thin films was characterized by X-ray diffraction (XRD) measurements at ambient temperature as shown in Fig. 1 left. The diffraction peaks with asterisks originate from the FTO conductive glass substrate while sharp reflection peaks located at $2\theta = 29.57°$, $36.45°$ and $42.33°$ represent the (110), (111) and (200) planes of Cu$_2$O, respectively. The XRD measurements revealed the formation of self-assembled cubic polycrystalline Cu$_2$O microstructure with a preferential orientation (111) in accordance with (ICDD PDF No. 01-071-3645).

It means that the nanostructures grow strongly in the perpendicular direction to the face (111). There is no diffraction peaks in the XRD spectrum related to the Cu or CuO confirming that the deposited film at the selected optimum conditions is a single phase cuprous oxide (Cu$_2$O). The average crystal size d of Cu$_2$O was calculated from XRD patterns using Debye–Scherrer formula [54]:

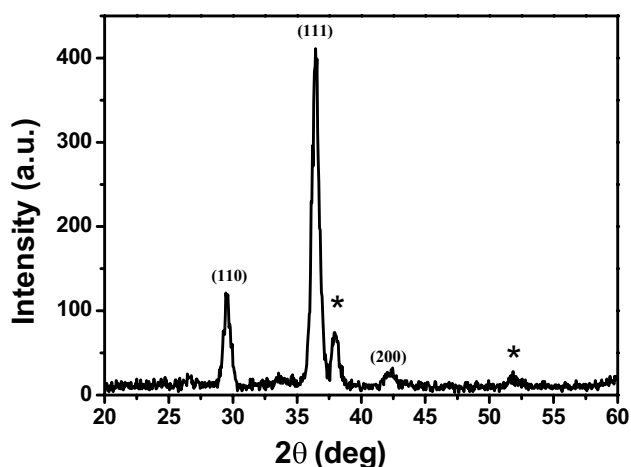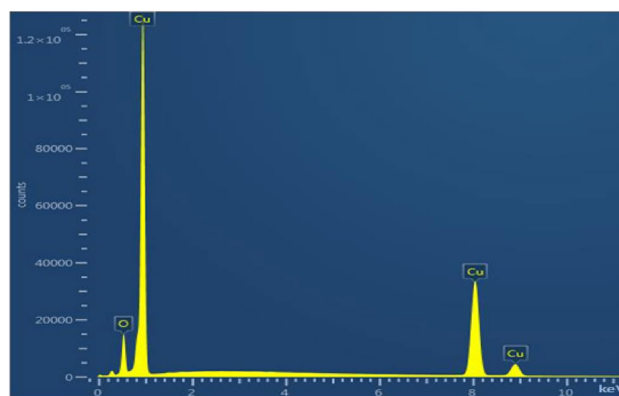$$D = \frac{0.9\lambda}{\beta\cos\theta} \tag{7}$$

Fig. 1 XRD diffraction pattern (left) and EDS spectra (right) of Cu_2O thin film electrodeposited on FTO substrate at room temperature. The XRD peaks marked with asterisks (*) refers to FTO substrate while the reflection peaks located at 2θ of 29.57°, 36.45° and 42.33° are related to Cu_2O (ICDD PDF No. 01-071-3645). The weight percentage for Cu and O from EDS are 91% and 9%, respectively

where λ (= 1.54056 Å) is the wavelength of the X-ray radiation, β is the full width at half maximum height (FWHM) of the diffraction peak in radians and 0.9 is the Scherrer constant for cubic symmetry. The peak position and FWHMs were determined by fitting the XRD spectrum with Gaussian distribution. The average crystal size calculated from the dominant (111) diffraction peak is about 12 nm in excellent agreement with previously reported data for electrodeposited Cu_2O on different substrates at pH 10 [42]. The density of dislocation ξ ($= 1/D^2$) is a parameter that gives information about the quality of crystallization as well as the crystal defects. The smaller dislocation density is the better crystallization of thin film. The calculated value of ξ for Cu_2O thin film is about 6.94×10^{-3} nm^{-2}. This smaller value indicates that the Cu_2O film has improved quality of crystallization.

The surface morphology of Cu_2O thin film is analyzed with scanning electron microscopy (SEM) and the image is shown in Fig. 2 left.

As clearly seen in the image, the p-Cu_2O grains are formed in a 3-sided pyramidal shape in the (111) growth direction on the FTO substrate. This means that at specific conditions of film preparation, the surface morphology is strongly linked with crystal surface. The number of hydroxyl ions is higher in the (111) orientation and hence greater concentration of oxygen atoms is available to form three-faced pyramidal crystallite in (111) preferred orientation. Wang et al. [55], reported similar behavior for electrodeposited Cu_2O films prepared at different pH values. They observed that when the pH values is above ~ 10.2, the (111) orientation with a three-faced pyramid grains becomes dominant.
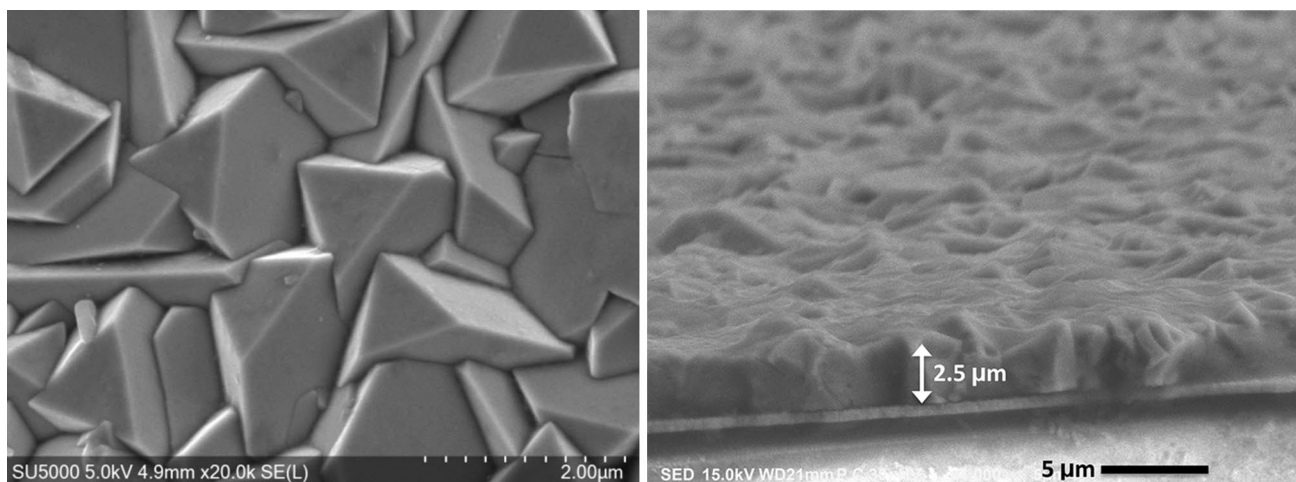

Fig. 2 Top view (left) and side view (right) SEM images of electrodeposited Cu_2O thin film on FTO substrate. Scale bar of top view and side view SEM images are 2 and 5 μm, respectively

They ascribed their findings to the increase of the concentration of oxygen atoms per unit area with increasing pH.

The average grain size obtained from SEM image is around 1.5 μm which is bigger than the calculated size from XRD. The difference in grain size may be due to the fact that the particles observed in SEM measurement contain multi-domains within the particle which is not the case in XRD measurement which reflects the crystalline domain size. In previous study [42], the structure and surface morphologies of Cu_2O films grown on different substrates at pH 10 were analyzed with XRD and SEM techniques and found that the grains of pyramidal shape corresponding to the (111) growth direction with an ITO substrate show average grain size of ~ 2 μm which is larger than that the XRD estimated size ($\sim$ 12 nm).

Elemental analysis of Cu_2O thin film is investigated by energy dispersive X-ray (EDS) to estimate the type and relative abundance of chemical elements present in the sample.

Figure 1 right shows EDS measurement for the as-prepared Cu_2O film taken at acceleration voltage of 30 kV. EDS results revealed the presence of copper and oxygen with relative ratios of 91% and 9%, respectively, which correspond to quasi-stoichiometric Cu_2O formed when exposed to air. These ratios are consistent with the expected theoretical percentage of Cu (88.81%) and O (11.18%) in Cu_2O. Similar results were reported for electrodeposited crystalline Cu_2O films with relative ratios of 88% for copper versus 12% for oxygen [56]. Overall, the (EDS) results confirm that the grown Cu_2O thin films are composed of copper and oxygen only.

3.2 Optical properties

The absorbance spectrum of Cu_2O thin films is shown in Fig. 3a.

Significant increase in absorbance is evident at wavelengths lower than 640 nm due to excitation and migration of electrons from the valence band to the conduction band. The appearance of the broad feature at about 700 nm in the absorption spectrum could possibly be due to the inter-band electron transition between the valence band and the conduction band. The optical band gap (E_g) of Cu_2O thin film can be determined based on the Beer–Lambert's law [57] (Eq. 8) and the model proposed by Tauc [58] (Eq. 9).

$$I = I_0 e^{-\alpha t} \tag{8}$$

$$(\alpha h v)^{1/n} = A\left(h v - E_g\right) \tag{9}$$

where I_0 and I are the incident and transmitted light intensity, t is the film thickness, α is the absorption coefficient, $h v$ is the photon energy and A is the band tailing parameter. Based on the nature of electronic transition responsible for
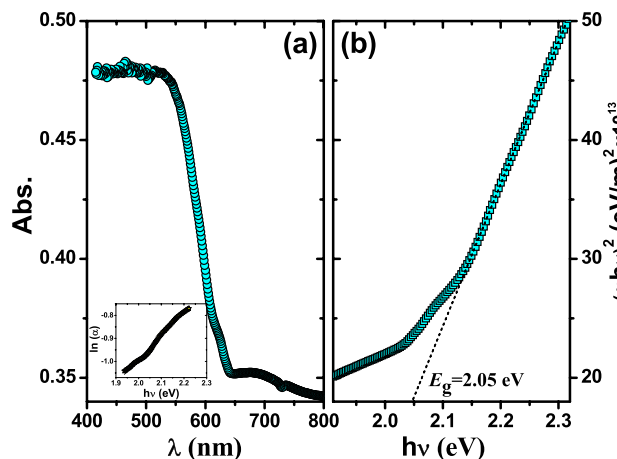

Fig. 3 **a** UV–Vis. absorbance spectra of electrodeposited Cu_2O thin film on FTO substrate. Inset: variation of ln (α) with $h v$ and the straight line represents the best fit from which the Urbach constant is obtained. **b** Corresponding plot of $(\alpha h v)^2$ against $h v$. The x-intercept at $(\alpha h v)^2 = 0$ of the line of best fit of the linear part of this graph gives the optical band gap, E_g

the absorption, the index n can have values of 1/2, 1/3, 2/3 and 2. It is found that $n = 1/2$ is the best fit for our results and is a characteristic of the direct allowed transition; which indicates that electrodeposited Cu_2O has a direct band gap. The x-axis intercept of the line of the best fit of the linear part of $(\alpha h v)^2$ against $h v$ at $(\alpha h v)^2 = 0$ gives the Cu_2O band gap of about 2.05 eV in excellent agreement with previously reported data by a number of authors [38, 42, 43] (Fig. 3b).

The Urbach energy (E_u) is defined as the energy width of the absorption edge and it is related to the absorption coefficient (α) by the following relation [59].

$$\alpha(v) = B \exp\left(\frac{h v}{E_u}\right) \tag{10}$$

where B is the low energy limit of absorption coefficient. By plotting the natural logarithm of α (lnα) as a function of photon energy ($h v$) (inset of Fig. 3a), one can determine the value of the Urbach energy by taking the slope at the linear region of the curve. The calculated value of E_u is 0.69 eV which is comparable to the recently published work by Bouderbala et al. [43].

The refractive index (n) and the optical energy gap (E_g) are interrelated through a formula proposed by Dimitrov and Sakka [60].

$$\frac{n^2 - 1}{n^2 + 2} = 1 - \sqrt{\frac{E_g}{20}} \tag{11}$$

Based on this relation, the refractive index of Cu_2O film is calculated and gives 2.71 in excellent agreement with most recently published results [43, 61].

Figure 4a shows the photoluminescence spectra of Cu_2O thin film measured in the temperature range 14–290 K. Three photoluminescence bands labeled as A, B and C is observed at photon energies of 1.47 eV ($\lambda \sim 843$ nm), 1.72 eV ($\lambda \sim 721$ nm) and 1.82 eV ($\lambda \sim 680$ nm), respectively. These bands are related to the recombination of bound excitons to copper vacancies (V_{Cu}^{1+}) (band A), single charged oxygen vacancies (V_O^{1+}) (band B) and double charged oxygen vacancies (V_O^{2+}) (band C).

These assignments are consistent with the previously reported data in the literature considering that the exact peak positions and its relative intensities are strongly depend on the used growth process as well as sample preparation [62–64]. Furthermore, the luminescent intensities for the three bands decrease exponentially with increasing temperature but in different reduction rates (Fig. 4b). For instance, the two luminescent bands related to the presence of oxygen vacancies demonstrate fast reduction rate in intensity with increasing temperature than that of the band due to the copper vacancies. The decrease in intensity of the absorption peak with increasing temperature is directly correlated with the reduction in the donor concentration (oxygen vacancies) and the formation of copper precipitates in the crystal [62]. The temperature dependence of the integrated intensity $I(T)$ of PL bands (Fig. 4b) can be well described by the following relation [65].

$$I(T) = \frac{I_0}{1 + \alpha \exp\left(-\frac{E_{PL}}{k_B T}\right)} \tag{12}$$

where α and E_{PL} are the rate parameter and activation energy, respectively. Equation (12) is used to fit the integrated intensity data for the bands located at $\lambda \sim 721$ nm (V_O^{1+}), 680 nm (V_O^{2+}) and 843 nm (V_{Cu}^{1+}) and the fitting parameters are compiled in Table 1.

The activation energies corresponding to the diffusion of oxygen vacancies were found to be 12.7 (V_O^{1+}) and 13.95 (V_O^{2+}) meV with pre-exponential factors of 41.5 and 61.7, respectively. The small difference in activation energies

Table 1 I_0, α and E_{PL} parameters obtained from the fitting of PL integrated intensity data (Fig. 4b) with Eq. (12) for Cu_2O thin film

| PL-band	I_0	α	E_{PL} (meV)
A (~ 1.47 eV) ($\lambda \sim 843$ nm)	1433	85.3	48.4
B (~ 1.72 eV) ($\lambda \sim 721$ nm)	2622	41.5	12.7
C (~ 1.82 eV) ($\lambda \sim 680$ nm)	3481	61.7	13.95

confirm that the defects responsible for the two bands at 1.72 and 1.82 eV are of the same origin but in different forms. On the other hand, the copper vacancies were found to diffuse with activation energy of 48.4 meV and pre-exponential factor of 85.3. This is approximately four times the values associated with the V_O^{1+} and V_O^{2+} defects. This might be due to the fact that the activation energy for copper vacancies might contain both the enthalpy of migration in addition to enthalpy for forming defect centers. Therefore, the activation energies obtained for oxygen vacancies is probably due to the migration enthalpy only. Moore and Selikson [66] have measured the diffusion of radiocopper in cuprous oxide stripes and found that the copper vacancies diffuse with activation energy twice that observed for the oxygen vacancies. Goldstein et al. [67] have developed a defect transport model to figure out the diffusion coefficient and activation energies of single charged copper vacancies in Cu_2O. They found that the copper vacancies diffuse in Cu_2O with activation energy of 0.56 eV which is consistence with our results.

3.3 Dielectric spectroscopy

The real part of AC-conductivity (σ') versus frequency at different temperatures is shown in Fig. 5a.

It is evident from the figure that the conductivity of Cu_2O is frequency and temperature dependent. Two frequency regions are distinguished: (i) the low frequency region in which the conductivity is frequency independent and DC contribution dominates and (ii) the high frequency region in which the conductivity increases monotonically with increasing frequency with apparent change in slope.

Fig. 4 **a** Photoluminescence (PL) spectra of Cu_2O thin film measured in the temperature range from 14 to 290 K. **b** The integrated PL peak intensity as a function of 1000/T. The solid lines in (**b**) represent the fitting according to Eq. (12)
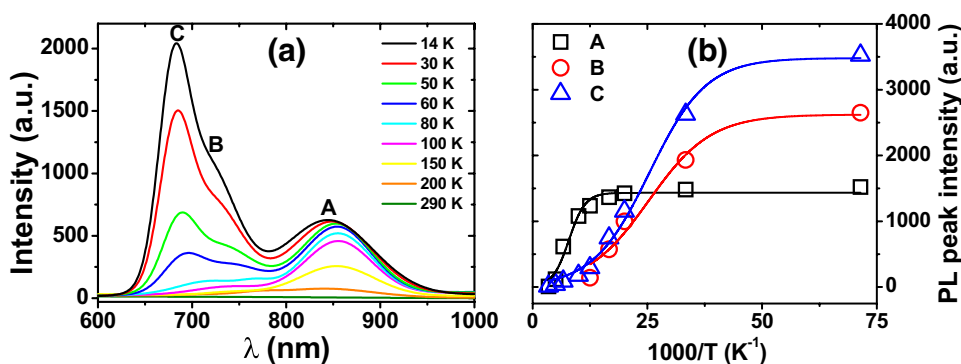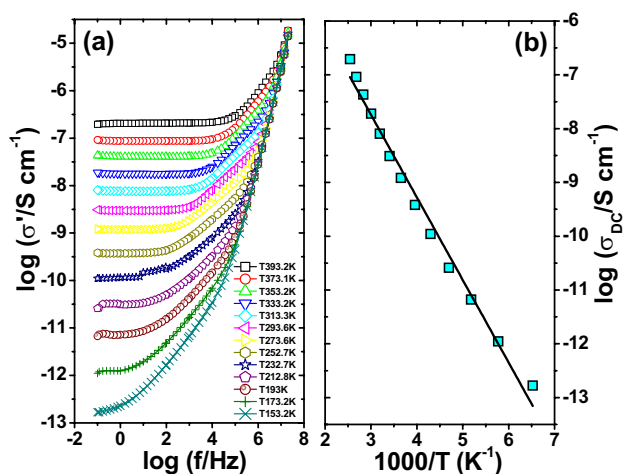
Fig. 5 **a** Frequency dependence of σ' at different temperatures (153–393 K) for Cu_2O thin film. **b** Temperature dependence of σ_{DC} extracted from the extrapolation of σ' curves (Fig. 5a) to lower frequencies ($f \rightarrow 0$). The solid line represents the fitting according to Arrhenius Eq. (14)

Fig. 6 **a** Dependence of ε' on frequency at different temperatures (153–393 K) for Cu_2O thin film. **b** Frequency dependence of the product $f\varepsilon''$ at selected temperatures. Inset is the temperature dependence of the frequency exponent s and the A constant. The solid line in the inset represents the fitting of s values with the CBH model

Transition from the low to high frequency regions occurs at critical frequency called the hopping frequency (ω_H) that shifts to higher frequencies with increasing temperature. The change in behavior in $\sigma'(\omega)$ from plane to rapidly rising may be related to a change in the hopping behavior of charge carriers from long range to short range [68]. The whole behavior can be described by the universal power law proposed by Jonscher [69].

$$\sigma'(\omega) = \sigma_{DC} + A\omega^s \qquad (13)$$

where σ_{DC} is the DC-conductivity, A and s are constants that depends on temperature. The frequency exponent s generally lies between zero and one.

Extrapolating the conductivity curves (Fig. 5a) to lower frequencies ($f \rightarrow 0$) enables us to extract the DC-conductivity (σ_{DC}) values for each temperature. Figure 5b shows the relation between σ_{DC} and $1000/T$, where T is the absolute temperature. As clearly seen in the figure, the σ_{DC} follows the Arrhenius temperature dependence [70].

$$\sigma_{DC} = \sigma_0 \exp\left(-\frac{E}{k_B T}\right) \qquad (14)$$

with a single activation energy $E = 0.3 \pm 0.01$ eV and pre-exponential factor (representing σ_{DC} at infinite temperature) $\sigma_0 = 7 \times 10^{-4}$ S cm^{-1}. This value is typical for bulk semiconductors and it is related to a single acceptor type impurities (p-type) as reported by Weichman et al. [71]. The p-type conduction mechanism in Cu_2O was investigated by Nolan and Elliot [72] using plane wave density functional theory (DFT) and DFT-U. They found that the holes formed due to the removal of copper atoms are responsible to the p-type
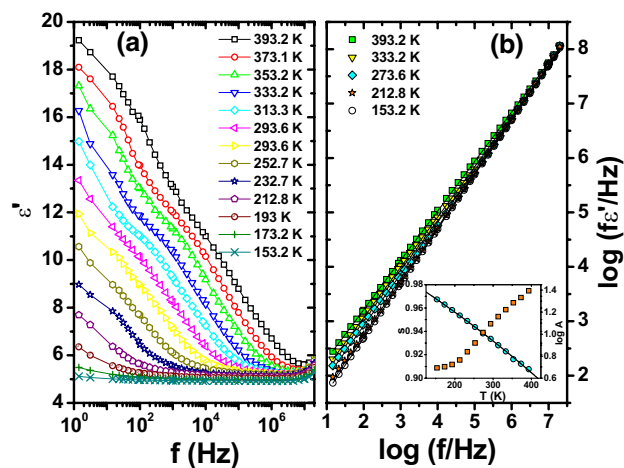
conduction properties and the formation energy of a Cu vacancy was found to be in the order of 0.4–1.7 eV.

Frequency dependence of the dielectric constant (ε') at different temperatures is depicted in Fig. 6a. The dielectric constant ε' shows both frequency and temperature dependence. It decreases with increasing frequency while it increases with increase in temperature. The rapid increase of ε' at very low frequencies is attributed to the build-ups of charge carriers at the Cu_2O grain boundaries. This phenomenon is known as the Maxwell–Wagner effect [46]. At higher frequencies, ε' approaches a constant value because dipoles cannot follow the rapid variation of the alternating electric filed.

To investigate the frequency dependent dielectric response caused by hopping charge carriers, the Jonscher's power law can be expressed by the following relation [52, 69],

$$\varepsilon' = \frac{\tan(s\pi/2)\sigma_0(T)}{\varepsilon_0} f^{s(T)-1} = A(T) f^{s(T)-1} \qquad (15)$$

where f is the applied frequency. Figure 6b shows the product $f\varepsilon'$ as a function of frequency in a log–log plot at selected temperatures. The values of A constant and frequency exponent s are obtained from the fitting of $f\varepsilon'$ data with Jonscher's power law given in Eq. (15). The results are presented in the inset of Fig. 6b as a function of temperature. With increasing temperature, the s values decreases from 1 to 0.9 while $\log A$ increases from 0.69 to 1.39.

The electrical conduction mechanism in different materials can be explored from the temperature and frequency dependent of the frequency exponents. Different

theoretical models as quantum mechanical tunneling (QMT), classical hopping over barrier (HOB) and the correlated barrier hopping (CBH) were proposed to correlate the conduction mechanism of AC-conductivity with the frequency exponent s in amorphous semiconductors [73–75]. In our system, the s values follow the same temperature dependent as that of the CBH model. In this model, two electrons or holes simultaneously hop over potential barrier between two charged defect states (D^+, D^-). The overlapping of the Coulomb well of the neighboring sites separated by distance R_ω, results in the lowering of the effective barrier height from W_M to W [75].

$$W = W_M - \frac{ne^2}{\pi\varepsilon'\varepsilon_0 R_\omega} \tag{16}$$

where W_M, R_ω, e and n are the maximum barrier height, the intersite separation (hopping distance), the electronic charge and the number of electrons participating in the hoping process, respectively. $n = 1$ for single polaron hopping and 2 for bipolaron hopping. The frequency exponent s in the CBH model is given by [75].

$$s = 1 - \frac{6k_B T}{W_M - k_B T \ln\left(\frac{1}{\omega\tau_0}\right)} \tag{17}$$

where k_B is the Boltzmann constant and τ_0 is the characteristic relaxation time. The frequency exponent s in the inset of Fig. 6b is fitted with Eq. (17) to get W_M and τ_0 at fixed value of frequency ω ($= 6.2 \times 10^7$ Hz). The fitting looks reasonably good over the temperature range under consideration and gives values of 2.58 ± 0.03 eV for W_M and 10^{-13} s for τ_0. The value of W_M can be associated with the maximum barrier height for bipolaron CBH as reported by a number of authors [47, 49, 76]. That means hopping between positive and negative defect centers (V_O^-, V_{Cu}^+) are responsible for the bipolaron conduction mechanism in Cu$_2$O. The best fitted values of W_M and τ_0 are used to calculate the effective barrier height W ($= k_B T \ln(1/\omega\tau_0)$) and the hopping distance between two neighboring sites R_ω at different frequencies according to Eq. (18).

$$R_\omega = \frac{2e^2}{\pi\varepsilon'\varepsilon_0 \left[W_M - k_B T \ln\left(\frac{1}{\omega\tau_0}\right)\right]} \tag{18}$$

The temperature dependence of R_ω at different frequencies is depicted in Fig. 7a.

It can be seen that R_ω is both temperature- and frequency-dependent. As the temperature increases, R_ω decreases and as the frequency increases, R_ω is increasing as predicted from Eq. (18). As a matter of fact, the increasing temperature tends to the overlapping of the Coulomb potential wells of the neighboring sites which leads to the lowering
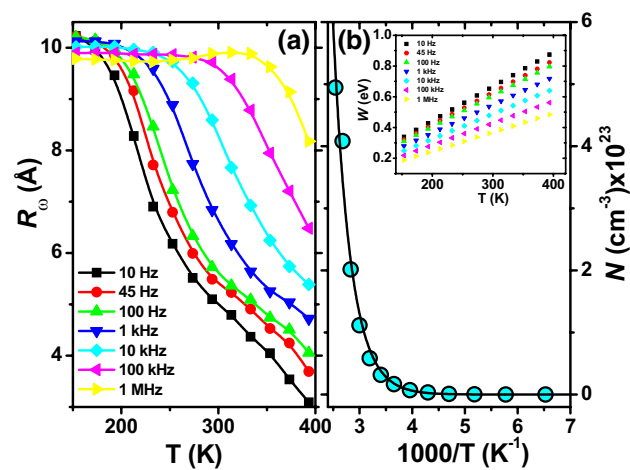

Fig. 7 Temperature dependence of the hopping distance R_ω at selected frequencies (**a**) and the charge carrier density N at frequency of 10 Hz (**b**) of Cu$_2$O thin film. R_ω and N are calculated based on Eqs. (18) and (19), respectively. The solid line on (**b**) represents the fitting according to Eq. (20). The inset of (**b**) is the effective barrier height (W) calculated at different frequencies

of the intersite separation distance (R_ω). On the other hand, increasing frequency will accelerate the rate of jumping of the bipolarons over the potential wells. The effective barrier height W (inset of Fig. 7b) has completely opposite trend to R_ω. It increases with increasing temperature and decrease with increasing frequency. A possible explanation for such behavior is that, as the temperature increases more electrons are thermally activated and have enough energy to overcome the potential barrier and as a result the effective barrier height W appears to increase with increasing temperature. Similar behavior was reported by Gupta et al. for Cu$_2$O/p-Si Schottky diode using the thermionic emission model [77]. In CBH model, the real part of AC-conductivity $\sigma'(\omega)$ is related to the density of charge carriers N according to the following relation [75].

$$\sigma'(\omega) = \frac{\pi^3}{24} N^2 \varepsilon\varepsilon_0 \omega R_\omega^6 \tag{19}$$

Figure 7b shows the temperature dependence of N at selected frequency of 10 Hz. The N values decreases exponentially with decreasing temperature and can be described by [71].

$$N = N_0 \exp\left(-\frac{E_a}{k_B T}\right) \tag{20}$$

where E_a is the energy required to ionize a natural acceptor to form a negative ion and hole. Using Eq. (20) to fit the calculated data of N, we estimate E_a to be 0.26 ± 0.02 eV. This ionization energy is in excellent agreement with the activation energy obtained from the conductivity (Fig. 5b)

and in agreement with previously reported experimental values for Cu_2O [78–81].

Frequency dependence of the dielectric loss ε'' at selected temperatures (253–393 K) is depicted in Fig. 8a. A single relaxation process named as β_2 is evident in the high frequency side of ε'' followed by an increase at lower frequencies. The latter is attributed to the DC electric conduction which increases with increasing temperature.

The β_2-relaxation process gains intensity and moves to higher frequencies with increasing temperature. Single HN function including the conductivity term (Eq. 21) is used to fit the isothermal dielectric loss spectra (Fig. 8a) and the relaxation times at peak maximum (τ_{max}) as well as HN-broadening parameters (α and $\alpha\gamma$) are extracted [82].

$$\varepsilon''(\omega) = \frac{\sigma_0}{\omega\varepsilon_0} - \sum_{j=1}^{n} Im\left[\frac{\Delta\varepsilon_j}{\left[1 + \left(i\omega\tau_{jHN}\right)^{\alpha_j}\right]^{\gamma_j}}\right] \quad (21)$$

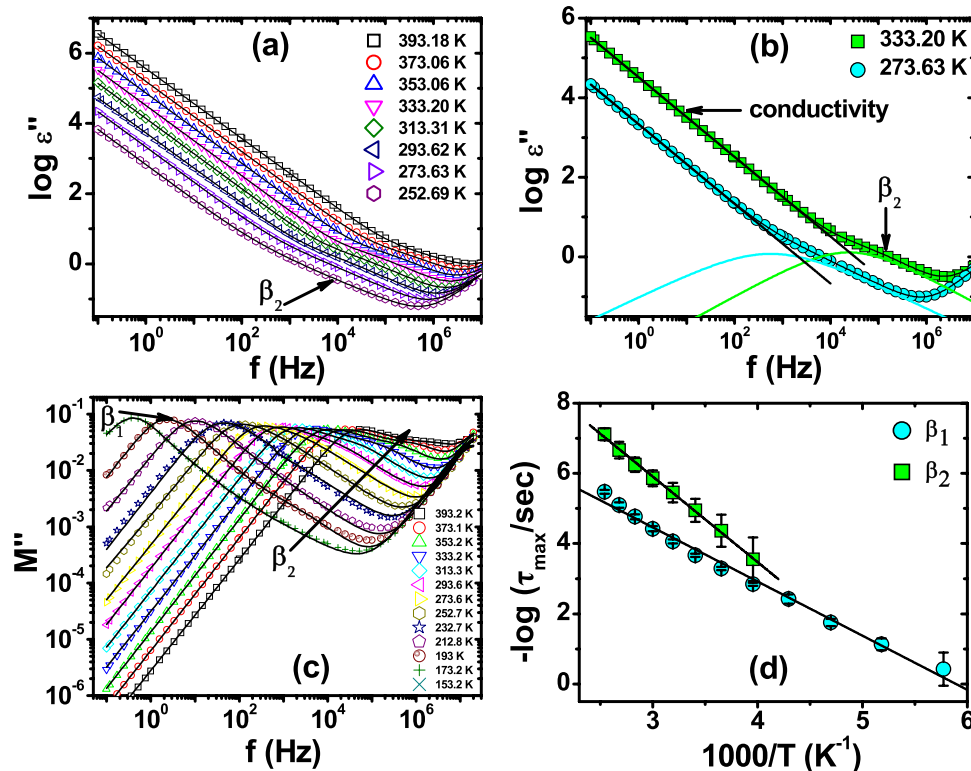Figure 8b shows some representative individual fits for the high frequency β_2-process at two selected temperatures (273.63 and 333.2 K). The HN-broadening parameters α and $\alpha\gamma$ for β_2-relaxation process are compiled in Table 2 at different temperatures.

The values of α and $\alpha\gamma$ are systematically decreasing with decreasing temperature for β_2-process. Beside the shape parameters, the relaxation times at maximum τ_{max} are obtained to generate the Arrhenius relaxation map by plotting τ_{max} versus the reciprocal of the peak temperature (Fig. 8d). An activation energy of 0.48 ± 0.01 eV with pre-exponential factors of $\tau_0 = 4.65 \times 10^{-13}$ s is obtained from the linear fit with Eq. (3).

Complex electric modulus M^* is related to the complex permittivity ε^* through Eq. 5. The advantage of presenting the dielectric relaxations in modulus formalism is that the effects of electrode polarization are completely suppressed. Furthermore, overwhelmed relaxation peaks due large values of ε' and ε'' at lower frequencies are completely eliminated.

Figure 8c shows the spectra of the imaginary part of electric modulus (M'') as a function of frequency at selected temperature. Two relaxation processes named as β_1 and β_2 are

Fig. 8 **a** Dielectric loss spectra ε'' for Cu_2O thin film at selected temperatures (253–393 K). Solid lines represent the fittings with a single HN function including the conductivity contribution (Eq. 21). For clarity, the individual fit for the high frequency process is shown in (**b**) at two temperatures of 273.63 K and 333.2 K. At these two temperatures the deconvolution of the spectra are shown with the solid cyan (273.63 K) and green lines. **c** Imaginary part of electric modulus M'' as a function of frequency at different temperatures (153–393 K). Solid lines represent the fittings to the β_1 and β_2 relaxation processes with two HN functions (Eq. 21). **d** Arrhenius relaxation map for the β_1 (circles) and β_2 (squares) relaxation processes. Solid lines in (**d**) represent the Arrhenius fits for β_1 and β_2 according to Eq. (3) giving activation energies of 0.31 ± 0.01 and 0.48 ± 0.01 eV, respectively (Color figure online)

Table 2 Havriliak–Negami (HN) broadening parameters α and $\alpha\gamma$ for β_1- and β_2- relaxation processes of Cu_2O thin film at different temperatures

T (K)	β_1-process		β_2-process	
	α	$\alpha\gamma$	α	$\alpha\gamma$
153.2	1	0.34	–	–
173.2	1	0.38	–	–
193	1	0.42	–	–
212.8	1	0.45	–	–
232.7	1	0.46	0.70	0.70
252.7	1	0.50	0.73	0.73
273.6	1	0.51	0.74	0.74
293.6	1	0.50	0.75	0.75
313.3	1	0.49	0.78	0.78
333.2	1	0.49	0.78	0.78
353.2	1	0.45	0.81	0.81
373.1	1	0.40	0.90	0.90
393.2	1	0.38	0.99	0.99

observed. The high frequency/high temperature β_2 process is the same relaxation process appeared in the ε'' representation while the low frequency relaxation process β_1 is appeared in the whole temperature range. Two HN-functions (Eq. 6) are employed to analyze the spectra and the corresponding relaxation times and shape parameters of the two processes are given in Fig. 8d; Table 2, respectively.

The shape parameters and relaxation rates obtained from M'' and ε'' representations are quite similar for β_2 relaxation process. The relaxation times for β_1 process has an Arrhenius temperature dependence with activation energy $E = 0.31 \pm 0.01$ eV and pre-exponential factors of $\tau_0 = 8 \times 10^{-10}$ s. This activation energy is in excellent agreement with the value obtained from Arrhenius plot for electrical conductivity given in Fig. 5b.

A remaining question is what is the relaxing species of β_1 and β_2? It is known that defects in most oxides are related to oxygen vacancies which serve as donors that create conductive electrons through ionization. Electrons can hop between positive and negative surface defect centers (V_O^-, V_{Cu}^+) giving rise to dipolar effect. Therefore, the characteristic relaxation times of the conductivity relaxation (β_1-process) are related to the hopping of the oxygen and copper vacancies. The Cu_2O form three-sided pyramidal grains with grain size of $\sim 1.5\ \mu$m. Such mesoscopic inhomogeneities are known to cause Maxwell–Wagner-Sillars (MWS) polarization effect [46]. Models of this type of effect consider the conductive Cu_2O grains embedded in a matrix of lower conductivity and separated by insulating grain boundaries. Consequently, an AC electric field induces a spatial separation of charge carriers within the grains exhibiting higher electrical conductivity in their interior than on their surface. Furthermore, the MWS is characterized by high dielectric strength ($\Delta\varepsilon \gg 1$). In our case $\Delta\varepsilon \sim 5$. Therefore, we argue that the β_2-relaxation

process is due to the Maxwell–Wagner-Sillars (MWS) polarization. This process was observed in CuO [48], TiO_2 [83] and NiO [84].

4 Conclusion

Cuprous oxide (Cu_2O) thin film was electrodeposited on FTO conducting substrate by the reduction of copper lactate in alkaline solution at pH = 12.25. Structural investigations by means of XRD, (EDS) and SEM confirmed the formation of self-assembled cubic microstructure of Cu_2O with average grain size of about 1.5 μm. The UV–Vis absorbance spectrum gives optical energy gap of 2.05 eV. The PL spectrums revealed the presence of defect centers ascribed to various forms of oxygen (V_O^{1+}, V_O^{2+}) and copper (V_{cu}) vacancies which were responsible for the conduction in Cu_2O thin film. The three waves emission related to vacancy defects (V_O^{1+}, V_O^{2+}, V_{Cu}^{1+}) show temperature dependence with different activation energies of diffusion. The conduction mechanism in Cu_2O thin film was successfully described by the CBH model in which bipolaron hopping was dominated. The density of defect states N, the effective barrier height W and the hopping distance R_ω were calculated based on the CBH model. Two dielectric relaxation processes β_1 and β_2 with Arrhenius temperature dependence and activation energies of 0.31 and 0.48 eV were detected. The high-temperature/high frequency β_2 relaxation process with activation energy of 0.48 eV was attributed to the MWS polarization while the conductivity relaxation process (β_1) with activation energy of 0.31 eV was related to the hopping of the oxygen and copper vacancies.

References

1. S. Sun, X. Zhang, Q. Yang, S. Liang, X. Zhang, Z. Yang, Prog. Mater Sci. **96**, 111–173 (2018). https://doi.org/10.1016/j.pmatsci.2018.03.006
2. X. Li, H. Gao, C.J. Murphy, L. Gou, Nano Lett. **4**, 1903–1907 (2004). https://doi.org/10.1021/nl048941n
3. Y. Qian, F. Ye, J. Xu, Z.G. Le, Int. J. Electrochem. Sci. **7**, 10063–10073 (2012)
4. P. Poizot, S. Laruelle, S. Grugeon, L. Dupont, J. Tarascon, Nature **407**, 496 (2000). https://doi.org/10.1038/35035045
5. J. Kondo, Chem. Commun. (1998). https://doi.org/10.1039/a707440i
6. B. Lefez, M. Lenglet, Chem. Phys. Lett. **179**, 223–226 (1991). https://doi.org/10.1016/0009-2614(91)87027-9
7. D. Snoke, Science **273**, 1351–1352 (1996). https://doi.org/10.1126/science.273.5280.1351

8. A. Musa, T. Akomolafe, M. Carter, Sol. Energy Mater. Sol. Cells **51**, 305–316 (1998). https://doi.org/10.1016/S0927-0248(97)00233-X

9. J. Zhang, J. Liu, Q. Peng, X. Wang, Y. Li, Chem. Mater. **18**, 867–871 (2006). https://doi.org/10.1021/cm052256f

10. M. Abdelfatah, J. Ledig, A. El-Shaer, A. Wagner, A. Sharafeev, P. Lemmens, M.M. Mosaad, A. Waag, A. Bakin, Sol. Energy **122**, 1193–1198 (2015). https://doi.org/10.1016/j.solener.2015.11.002

11. M. Abdelfatah, J. Ledig, A. El-Shaer, A. Wagner, V. Marin-Borras, A. Sharafeev, P. Lemmens, M.M. Mosaad, A. Waag, A. Bakin, Sol. Energy Mater. Sol. Cells **145**, 454–461 (2016). https://doi.org/10.1016/j.solmat.2015.11.015

12. Y. Yang, M. Pritzker, Y. Li, Thin Solid Films **676**, 42–53 (2019). https://doi.org/10.1016/j.tsf.2019.02.014

13. B. Balamurugan, B. Mehta, Thin Solid Films **396**, 90–96 (2001). https://doi.org/10.1016/S0040-6090(01)01216-0

14. D.A. Firmansyah, T. Kim, S. Kim, K. Sullivan, M.R. Zachariah, D. Lee, Langmuir **25**, 7063–7071 (2009). https://doi.org/10.1021/la9001175

15. P. Liu, Z. Li, W. Cai, M. Fang, X. Luo, RSC Adv. **1**, 847–851 (2011). https://doi.org/10.1039/C1RA00261A

16. K. Suzuki, N. Tanaka, A. Ando, H. Takagi, J. Am. Ceram. Soc. **94**, 2379–2385 (2011). https://doi.org/10.1111/j.1551-2916.2011.04413.x

17. R.V. Kumar, Y. Mastai, Y. Diamant, A. Gedanken, J. Mater. Chem. **11**, 1209–1213 (2001). https://doi.org/10.1039/b005769j

18. M.A. Bhosale, K.D. Bhatte, B.M. Bhanage, Powder Technol. **235**, 516–519 (2013). https://doi.org/10.1016/j.powtec.2012.11.006

19. B. Yadav, A. Yadav, Int. J. Green Nanotechnol. **1**, M16–M31 (2009). https://doi.org/10.1080/19430840902931541

20. Y. Sui, Y. Zeng, W. Zheng, B. Liu, B. Zou, H. Yang, Sens. Actuators B **171**, 135–140 (2012). https://doi.org/10.1016/j.snb.2012.01.069

21. L. Gou, C.J. Murphy, J. Mater. Chem. **14**, 735–738 (2004). https://doi.org/10.1039/B311625E

22. Y. Bai, T. Yang, Q. Gu, G. Cheng, R. Zheng, Powder Technol. **227**, 35–42 (2012). https://doi.org/10.1016/j.powtec.2012.02.008

23. M.H. Huang, C.-Y. Chiu, J. Mater. Chem. A **1**, 8081–8092 (2013). https://doi.org/10.1016/j.powtec.2012.02.008

24. L. Gou, C.J. Murphy, Nano Lett. **3**, 231–234 (2003). https://doi.org/10.1021/nl0258776

25. Stareck JE (1941) Google Patents, 1941. https://patents.google.com/patent/US2250556A/en

26. G. Riveros, A. Garmendia, D. Ramirez, M. Tejos, P. Grez, H. Gomez, E. Dalchiele, J. Electrochem. Soc. **160**(1), D28–D33 (2013)

27. S. Laidoudi, A. Bioud, A. Azizi, G. Schmerber, J. Bartringer, S. Barre, A. Dinia, Semicond. Sci. Technol. **28**, 115005 (2013). https://doi.org/10.1088/0268-1242/28/11/115005

28. S. Barman, D. Sarma, J. Phys. **4**, 7607 (1992). https://doi.org/10.1088/0953-8984/4/37/008

29. Z.-X. Shen, R. List, D. Dessau, F. Parmigiani, A. Arko, R. Bartlett, B. Wells, I. Lindau, W. Spicer, Phys. Rev. B **42**, 8081 (1990). https://doi.org/10.1103/PhysRevB.42.8081

30. A. Önsten, M. Månsson, T. Claesson, T. Muro, T. Matsushita, T. Nakamura, T. Kinoshita, U.O. Karlsson, O. Tjernberg, Phys. Rev. B **76**, 115127 (2007). https://doi.org/10.1103/PhysRevB.76.115127

31. A. Jolk, C. Klingshirn, Physica Status Solidi (b) **206**, 841–850 (1998). https://doi.org/10.1002/(SICI)1521-3951

32. C. Uihlein, D. Fröhlich, R. Kenklies, Phys. Rev. B **23**, 2731 (1981). https://doi.org/10.1002/(SICI)1521-3951(199804)206:2%3c841:AID-PSSB841%3e3.0.CO;2-N

33. N. Serin, T. Serin, Ş. Horzum, Y. Celik, Semicond. Sci. Technol. **20**, 398 (2005). https://doi.org/10.1088/0268-1242/20/5/012

34. M. Beg, S. Shapiro, Phys. Rev. B **13**, 1728 (1976). https://doi.org/10.1103/PhysRevB.13.1728

35. R. Mittal, S. Chaplot, S. Mishra, P.P. Bose, Phys. Rev. B **75**, 174303 (2007). https://doi.org/10.1103/PhysRevB.75.174303

36. E. Ruiz, S. Alvarez, P. Alemany, R.A. Evarestov, Phys. Rev. B **56**, 7189 (1997). https://doi.org/10.1103/PhysRevB.56.7189

37. D.O. Scanlon, G.W. Watson, Phys. Rev. Lett. **106**, 186403 (2011). https://doi.org/10.1103/PhysRevLett.106.186403

38. X. Jiang, M. Zhang, M. Shi, G. He, X. Song, Z. Sun, Nanoscale Res. Lett. **9**, 219 (2014). https://doi.org/10.1186/1556-276X-9-219

39. C. Das, A.K. Singh, Y. Heo, G. Aggarwal, S.K. Maurya, J. Seidel, B. Kavaipatti, J. Phys. Chem. C **122**, 1466–1476 (2018). https://doi.org/10.1021/acs.jpcc.7b10103

40. J. Major, Y. Proskuryakov, K. Durose, G. Zoppi, I. Forbes, Sol. Energy Mater. Sol. Cells **94**, 1107–1112 (2010). https://doi.org/10.1016/j.solmat.2010.02.034

41. J. Chen, T. Shi, X. Li, B. Zhou, H. Cao, Y. Wang, Appl. Phys. Lett. **108**, 053302 (2016). https://doi.org/10.1063/1.4941238

42. Y. Liu, Y. Liu, R. Mu, H. Yang, C. Shao, J. Zhang, Y. Lu, D. Shen, X. Fan, Semicond. Sci. Technol. **20**, 44 (2004). https://doi.org/10.1088/0268-1242/20/1/

43. I.Y. Bouderbala, A. Herbadji, L. Mentar, A. Beniaiche, A. Azizi, J. Electron. Mater. **47**, 2000–2008 (2018). https://doi.org/10.1007/s11664-017-6001-z

44. O. Reyes, D. Maldonado, J. Escorcia-García, P. Sebastian, J. Mater. Sci. (2018). https://doi.org/10.1007/s10854-018-9110-4

45. M. Takahata, N. Naka, Phys. Rev. B **98**, 195205 (2018). https://doi.org/10.1103/PhysRevB.98.195205

46. A. Schönhals, F. Kremer, *Analysis of dielectric spectra* (Broadband dielectric spectroscopy. Springer, Heidelberg, 2003), pp. 59–98

47. J. Koshy, S.M. Soosen, A. Chandran, K. George, J. Semicond. **36**, 122003 (2015). https://doi.org/10.1088/1674-4926/36/12/122003

48. S. Sarkar, P.K. Jana, B. Chaudhuri, H. Sakata, Appl. Phys. Lett. **89**, 212905 (2006). https://doi.org/10.1063/1.2393001

49. K. Deepthi, T. Pandiyarajan, B. Karthikeyan, J. Mater. Sci. **24**, 1045–1051 (2013). https://doi.org/10.1007/s10854-012-0875-6

50. T. Serin, A. Yildiz, Ş.H. Şahin, N. Serin, Physica B **406**, 575–578 (2011). https://doi.org/10.1016/j.physb.2010.11.044

51. T. Serin, A. Yildiz, Ş. Şahin, N. Serin, Physica B **406**, 3551–3555 (2011). https://doi.org/10.1016/j.physb.2011.06.021

52. Q. Li, M. Xu, H. Fan, H. Wang, B. Peng, C. Long, Y. Zhai, Mater. Sci. Eng., B **178**, 496–501 (2013). https://doi.org/10.1016/j.mseb.2013.02.004

53. McCrum NG, Read BE, Williams G (1967) Doi: 10.1002/app.1969.070130214

54. Cullity B, Stock S (2001) Elements of x-ray diffraction 167–171. ISBN-13: 978-0201610918

55. L. Wang, N. De Tacconi, C. Chenthamarakshan, K. Rajeshwar, M. Tao, Thin Solid Films **515**, 3090–3095 (2007). https://doi.org/10.1016/j.tsf.2006.08.041

56. A.H. Alami, A. Allagui, H. Alawadhi, Renew. Energy **82**, 21–25 (2015). https://doi.org/10.1016/j.renene.2014.08.040

57. A.J. Nozik, G. Conibeer, M.C. Beard, *Advanced concepts in photovoltaics* (Royal Society of Chemistry, London, 2014)

58. J. Tauc, R. Grigorovici, A. Vancu, Physica Status Solidi (b) **15**, 627–637 (1966). https://doi.org/10.1002/pssb.19660150224

59. F. Urbach, Phys. Rev. **92**, 1324 (1953). https://doi.org/10.1103/PhysRev.92.1324

60. V. Dimitrov, S. Sakka, J. Appl. Phys. **79**, 1741–1745 (1996). https://doi.org/10.1063/1.360963

61. S. Pelegrini, M.A. Tumelero, I.S. Brandt, R.D. Pace, R. Faccio, A. Pasa, J. Appl. Phys. **123**(16), 161567 (2018). https://doi.org/10.1063/1.5004782

62. C. Teh, F. Weichman, Can. J. Phys. **61**, 1423–1427 (1983). https://doi.org/10.1139/p83-182

63. H. Solache-Carranco, G. Juárez-Díaz, A. Esparza-García, M. Briseño-García, M. Galván-Arellano, J. Martínez-Juárez, G. Romero-Paredes, R. Peña-Sierra, J. Lumin. **129**, 1483–1487 (2009). https://doi.org/10.1016/j.jlumin.2009.02.033

64. T. Ito, T. Masumi, J. Phys. Soc. Jpn. **66**, 2185–2193 (1997). https://doi.org/10.1143/JPSJ.66.2185

65. J. Krustok, H. Collan, K. Hjelt, J. Appl. Phys. **81**, 1442–1445 (1997). https://doi.org/10.1063/1.363903

66. W.J. Moore, B. Selikson, J. Chem. Phys. **19**, 1539–1543 (1951). https://doi.org/10.1063/1.1748118

67. E.A. Goldstein, T.M. Gür, R.E. Mitchell, Corros. Sci. **99**, 53–65 (2015). https://doi.org/10.1016/j.corsci.2015.05.067

68. A.A. Ali, M.M. Elmahdy, A. Sarhan, M.I. Abdel Hamid, M.T. Ahmed, Polym. Int. **67**, 1615–1628 (2018). https://doi.org/10.1002/pi.5685

69. A.K. Jonscher, *Universal relaxation law: a sequel to dielectric relaxation in solids* (Chelsea Dielectrics Press, Chelsea, 1996)

70. I.M. El-Sherbiny, M.M. Elmahdy, J. Appl. Polym. Sci. **118**, 2134–2145 (2010). https://doi.org/10.1002/app.32517

71. R. Kužel, F. Weichman, J. Appl. Phys. **41**, 271–279 (1970). https://doi.org/10.1063/1.1658333

72. M. Nolan, S.D. Elliott, Phys. Chem. Chem. Phys. **8**, 5350–5358 (2006). https://doi.org/10.1039/B611969G

73. P. Extance, S. Elliott, E. Davis, Phys. Rev. B **32**, 8148 (1985). https://doi.org/10.1103/PhysRevB.32.8148

74. A. Long, Adv. Phys. **31**, 553–637 (1982). https://doi.org/10.1080/00018738200101418

75. S. Elliott, Adv. Phys. **36**, 135–217 (1987). https://doi.org/10.1080/00018738700101971

76. G.-M. Zhao, M. Hunt, H. Keller, K. Müller, Nature **385**, 236 (1997). https://doi.org/10.1038/385236a0

77. R. Gupta, K. Ghosh, P. Kahol, Physica E **41**, 876–878 (2009). https://doi.org/10.1016/j.physe.2008.12.025

78. Y.S. Lee, M.T. Winkler, S.C. Siah, R. Brandt, T. Buonassisi, Appl. Phys. Lett. **98**, 192115 (2011). https://doi.org/10.1063/1.3589810

79. S. Ishizuka, S. Kato, T. Maruyama, K. Akimoto, Jpn. J. Appl. Phys. **40**, 2765 (2001). https://doi.org/10.1143/JJAP.40.2765

80. K. Matsuzaki, K. Nomura, H. Yanagi, T. Kamiya, M. Hirano, H. Hosono, Physica Status Solidi (a) **206**(9), 2192–2197 (2009). https://doi.org/10.1002/pssa.200881795

81. G. Pollack, D. Trivich, J. Appl. Phys. **46**, 163–172 (1975). https://doi.org/10.1063/1.321312

82. W.K. Kipnusu, M.M. Elmahdy, M. Elsayed, R. Krause-Rehberg, F. Kremer, Macromolecules **52**, 1864–1873 (2019). https://doi.org/10.1021/acs.macromol.8b02687

83. C. Wang, N. Zhang, Q. Li, Y. Yu, J. Zhang, Y. Li, H. Wang, J. Am. Ceram. Soc. **98**, 148–153 (2015). https://doi.org/10.1111/jace.13250

84. R. Karsthof, M. Grundmann, A.M. Anton, F. Kremer, Phys. Rev. B **99**, 235201 (2019). https://doi.org/10.1103/PhysRevB.99.235201